Journal of Materials Chemistry A

PAPER

View Article Online
View Journal | View Issue

Cite this: J. Mater. Chem. A, 2016, 4, 15041

Pitaya-like microspheres derived from Prussian blue analogues as ultralong-life anodes for lithium storage†

Lianbo Ma,‡[a] Tao Chen,‡[a] Guoyin Zhu,‡[a] Yi Hu,[a] Hongling Lu,[a] Renpeng Chen,[a] Jia Liang,[a] Zuoxiu Tie,[a] Zhong Jin*[a] and Jie Liu*[ab]

Received 5th August 2016
Accepted 5th September 2016

DOI: 10.1039/c6ta06692e

www.rsc.org/MaterialsA

To alleviate the capacity degradation of conventional anode materials caused by serious volume expansion and particle aggregation for lithium-ion batteries (LIBs), considerable attention has been devoted to the rational design and synthesis of novel anode architectures. Herein, we report an effective fabrication strategy to implant well-distributed carbide nanoparticles into spherical porous carbon frameworks to form pitaya-like microspheres. Benefiting from their unique components and architecture features, the as-synthesized pitaya-like microspheres can effectively buffer the volume change and prevent aggregation of Co_3ZnC nanoparticles during the charge/discharge processes of LIBs. The porous carbon framework provides an unhindered pathway for electron transport and Li^+ diffusion and restricts the thin solid-electrolyte interphase (SEI) layer to the outer surface of carbon outer-shells. In LIBs, the anodes deliver a high capacity of 608 mA h g^{-1} at 100 mA g^{-1} after 300 charge/discharge cycles and ultrahigh cyclic stability and rate performance with a capacity of 423 mA h g^{-1} even after 1150 consecutive cycles at 1000 mA g^{-1}.

Introduction

The ever increasing energy demand and environmental crisis call for efficient, clean, and sustainable sources of energy, and also advanced technologies associated with energy conversion and storage.[1–3] With the merits of relatively high power/energy density and conversion efficiency, long lifespan, and environmental benignity, lithium-ion batteries (LIBs) have attracted worldwide attention, and have been successfully adopted as the energy sources for a wide range of portable electronic devices, electric vehicles and hybrid electric vehicles.[4–10] However, conventional anode materials for LIBs usually suffer from volume expansion during charge/discharge processes and/or inferior rate capability,[11,12] which remain the major challenges for use in practical applications. In this regard, considerable efforts are urgently needed to the design and fabrication of attractive anode materials which can store and deliver energy more efficiently to improve the electrochemical performance of LIBs.[13,14]

Metal carbides are emerging as promising electrode materials for electrochemical storage devices including LIBs, supercapacitors and fuel cells due to their good electrical conductivity, high theoretical capacity and excellent stability.[15,16] In terms of energy storage, Gogotsi *et al.* demonstrated that the two-dimensional layered carbides (MXenes), such as Nb_2C,[17] TiC,[18,19] V_2C,[20] and Cr_2C[21] *etc.*, could be applied as anode materials for LIBs, and the Li^+ storage mechanism was found to be Li^+ intercalation and de-intercalation between the layers. Further theoretical calculations on two-dimensional layered metal carbides reported by Zhou *et al.* were consistent with the above results.[22] Moreover, Gogotsi and his co-workers also proved the promising application of layered carbides as supercapacitor electrode materials.[23] Although great progress has been achieved for the layered carbides in energy storage, non-layered carbides have also caught increasing attention due to their merits of relatively facile synthesis strategy, high surface area, good electrical conductivity, short ion diffusion paths and so on.[24–26] It is highly worthwhile to explore the possibility of non-layered metal carbide materials different from MXenes for effective energy storage, and these studies may pave the way for the further application of diverse metal carbides.

Active materials in the form of nanoscale particles usually exhibit high electrochemical reaction activity and a relatively high specific surface area. The high surface area of anode materials can obviously increase the interaction with the electrolyte, which is of significant importance for LIBs. However, nanostructured electrode materials usually suffer from vulnerability to oxidation and/or aggregation, thus severely suppressing their practical applications.[27,28] To circumvent these

[a]Key Laboratory of Mesoscopic Chemistry of MOE, Collaborative Innovation Center of Chemistry for Life Sciences, School of Chemistry and Chemical Engineering, Nanjing University, Nanjing, 210093, China. E-mail: zhongjin@nju.edu.cn; j.liu@duke.edu
[b]Department of Chemistry, Duke University, Durham, North Carolina, 27708, USA

† Electronic supplementary information (ESI) available. See DOI: 10.1039/c6ta06692e

‡ These authors contributed equally to this work.

obstacles, combining nanoscale active materials with a carbon matrix has been proved to be an effective strategy, which can obviously alleviate the oxidation and aggregation of bare nanoparticles.[29–32] As a result, the anodes can exhibit high discharge capacity and ultralong cyclic life.[33–36] In this respect, the design and construction of metal carbide particles containing a carbon matrix would be a promising way for developing innovative electrode materials based on non-layered metal carbides with improved energy storage performance.

Herein, we demonstrate that pitaya-like microspheres (Co_3ZnC/C) can be applied as ultralong-life anode materials in LIBs. A Prussian blue analogue (PBA) was selected as the precursor to provide two metal elements simultaneously, thus forming nanocomposites of bimetallic carbide and a carbon framework with unique components and architecture. In particular, by selecting appropriate PBA precursors, it is very convenient to obtain various bimetallic carbides or even multimetallic carbides with a homogeneous structure and highly diverse compositions, which then provide a unique opportunity to develop a new class of highly tunable functional materials. Moreover, among numerous bimetallic carbides, the Co_3ZnC material possesses good thermal stability and resistance against oxidation, relatively high electrical conductivity, and low cost. The three-dimensional (3D) porous and spherical carbon frameworks can buffer the volume change, prevent aggregation of carbide nanoparticles, and provide smooth pathways for electron transport and Li^+ diffusion during charge/discharge processes. As a consequence, the pitaya-like microspheres exhibit great electrochemical performance with ultrahigh cycling stability for LIBs.

Experimental

Chemicals and synthesis

All chemicals in this work are of analytical purity and used without further purification. The microsphere was synthesized according to our previous report with slight modifications.[37] Typically, 1.2 mmol of zinc acetate ($Zn(NO_3)_2 \cdot 6H_2O$) and 11.12 g of polyvinylpyrrolidone (PVP) were thoroughly dissolved in 40 mL of deionized water. Subsequently, 10 mL of 0.10 M $K_3[Co(CN)_6]$ aqueous solution was added into the above solution gradually under stirring and sonicated in a N_2 atmosphere at 45 °C. After that, the mixture was aged at 45 °C for 6 h without any disturbance. To get the final product, the as-obtained precipitate was first annealed at 300 °C for 1.0 h, and then at 600 °C for 2.0 h in a N_2 atmosphere with a ramping rate of 2.0 °C min^{-1}. Similarly, bare Co_3ZnC nanoparticles were prepared in the same way described above but without the introduction of PVP.

Instrumentation and characterization

The morphology, size and structure of the products were examined by field-emission scanning electron microscopy (FESEM, JSM-6480) and transmission electron microscopy (TEM, JEM-2100). Elemental analysis was performed using an energy-filtered TEM and an energy-dispersive X-ray spectroscope (EDX) attached to the FESEM. The crystallinity of the as-synthesized samples was characterized by powder X-ray diffraction (XRD) on a Bruker D-8 Advance diffractometer using Cu Kα ($\lambda = 1.5406$ Å) radiation at a scanning rate of 6° min^{-1}. Raman spectra were collected with a Horiba JY H800 Raman spectrometer using a 532 nm laser source. Thermogravimetric analysis (TGA) was conducted with an integrated thermal analyzer (NETZSCH STA449C) at a heating rate of 10 °C min^{-1} under air. Nitrogen adsorption–desorption isotherms were obtained through Brunauer–Emmett–Teller (BET) analysis at 77 K on a Micromeritics ASAP2020 instrument. X-ray photoelectron spectra (XPS) were recorded on a PHI-5000 VersaProbe X-ray photoelectron spectrometer using Al Kα X-ray radiation.

Electrochemical measurements

The working electrode consisted of the active material (pitaya-like microspheres or bare Co_3ZnC nanoparticles), carbon black, and binder (polyvinylidene difluoride, PVDF) in *N*-methy-pyrrolidinone (NMP) solvent with a weight ratio of 80 : 10 : 10. The loading mass of the active material was *ca.* 1.0–2.0 mg. The slurry was pasted onto a copper foil, and then dried at 110 °C overnight under vacuum. The electrochemical tests were carried out using CR2032 cells with lithium foil as the counter electrode at room temperature. The batteries were assembled in a glovebox filled with argon gas. The electrolyte is 1.0 M $LiPF_6$ in a mixture of ethylene carbonate and diethyl carbonate (1 : 1 in volume ratio). The electrochemical properties of LIBs were tested on a LAND battery test system (Wuhan LAND Electronics, China) within the voltage range of 0.01 to 3.0 V *vs.* Li/Li^+. Cyclic voltammetry (CV, 0.2 mV s^{-1}) and galvanostatic charge/discharge measurements were performed to investigate the electrochemical performance of pitaya-like microspheres. The reversible specific capacity of the anode was calculated based on the total loading weight of the active material.

Results and discussion

Formation of pitaya-like microspheres

In this work, we report the fabrication of pitaya-like microsphere nanoparticles embedded in spherical carbon frameworks by the controlled solution-phase synthesis of PBA precursor microspheres and the following moderate thermal annealing treatment. The synthesis process of the pitaya-like microspheres is presented in Fig. 1a. Firstly, $Zn(NO_3)_2$, PVP, and $K_3[Co(CN)_6]$ were used as the starting materials, and when the two solutions of $Zn(NO_3)_2$/PVP and $K_3[Co(CN)_6]$ were mixed together under ultrasonication, white nanoparticles were formed. After the mixture was aged, the nanoparticles aggregated together to form uniform microspheres. The XRD spectrum (Fig. S1†) confirmed that the as-formed precursor microspheres were composed of a PBA compound $Zn_3[Co(CN)_6]_2 \cdot nH_2O$. The PVP in the synthesis procedure acted as the capping agent for the formation of PBA precursor microspheres and greatly affected the morphology of the PBA precursor. With the decreasing amount of added PVP, the PBA precursor displayed a different structure, as illustrated in

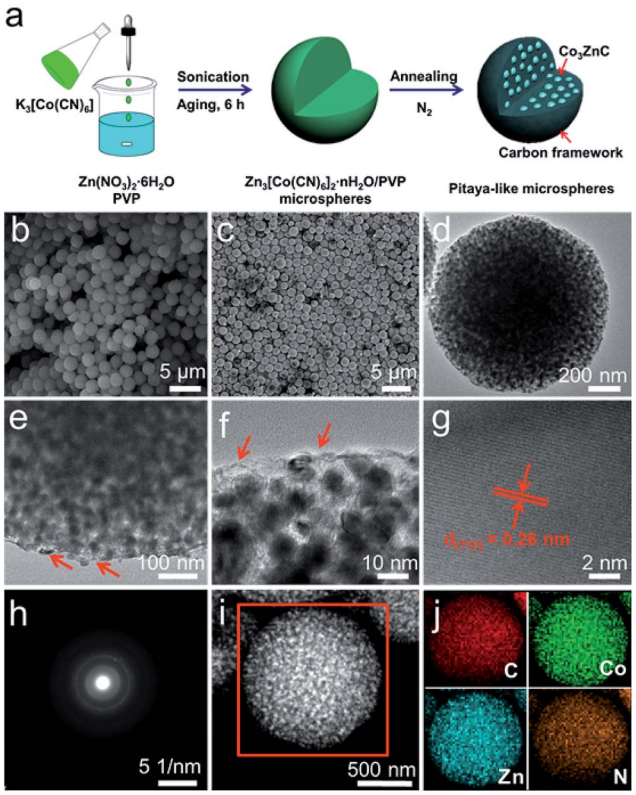

Fig. 1 Synthesis and morphology characterization of pitaya-like microspheres. (a) Schematic illustration of the formation process of pitaya-like microspheres. (b) FESEM image of $Zn_3[Co(CN)_6]_2{\cdot}nH_2O$/PVP precursor microspheres. (c) FESEM, (d–f) TEM, (g) high-resolution TEM and (h) SAED images of the as-synthesized pitaya-like microspheres, respectively. The rough edges of carbon outer-shells in (d) and (e) are marked by red arrows. The lattice distance in (g) is measured to be 0.26 nm, corresponding to the (110) planes of the cubic phase Co_3ZnC. (i) Energy-filtered TEM image of a pitaya-like microsphere and (j) the C, Co, Zn and N elemental mapping collected in the same rectangle area of (i), respectively.

Fig. S2.† To obtain the final product, the precursor microspheres were first annealed at 300 °C, and then at 600 °C in a N_2 atmosphere. This process promoted the gradual formation of Co_3ZnC and finally achieved the conversion of the PBA precursor into the ideal structure of pitaya-like microspheres.

Characterization of pitaya-like microspheres

The morphological and structural features of the PBA precursor microspheres and the pitaya-like microspheres were first characterized by field-emission scanning electron microscopy (FESEM) and transition electron microscopy (TEM). As shown in Fig. 1b, the PBA precursor obtained after aging clearly consists of uniform microspheres with a relatively smooth surface and a narrow diameter distribution range of 1.6–2.0 μm. Further TEM characterization (Fig. S3†) reveals the homogenous solid characteristics of PBA precursor microspheres. After the thermal treatment, the PBA precursor was converted into a bimetallic carbide/carbon composite with a highly porous structure and well-preserved morphology as monodispersed microspheres (Fig. 1c). The resultant pitaya-like microspheres are with a smaller size because of the shrinkage in the thermal annealing process. The interior fine structure of the as-prepared microspheres was examined by TEM. From Fig. 1d, it can be clearly seen that the microspheres are with a diameter of ~1.5 μm and possess discernible high-porosity. Besides, the surface of the microspheres became rougher, indicating that the microspheres were encapsulated by carbon outer-shells with plenty of nanopores, which is favorable for the penetration and migration of the electrolyte ions. Fig. 1e and f show TEM images with higher magnifications, the rough edges of carbon shells can be seen clearly, as marked by red arrows. In the product microspheres, nanoparticles with a size range of 10–15 nm were distributed uniformly inside the carbon frameworks, while no nanoparticles aggregated together. This special architecture can greatly reduce the volume expansion during the charge/discharge process and prevent the aggregation of the active material without hindering electron transport and Li^+ diffusion, thus resulting in enhanced electrochemical performance.[38,39] The high-resolution TEM characterization of the encapsulated nanoparticles (Fig. 1g) revealed a lattice distance of 0.26 nm, corresponding to the (110) planes of the cubic phase Co_3ZnC. The selected-area electron diffraction (SAED) pattern of pitaya-like microspheres (Fig. 1h) demonstrates the polycrystalline nature of the sample. To investigate the elemental distribution in the microspheres, elemental mapping of a selected area (the rectangle area in Fig. 1i) is provided by energy-filtered TEM in Fig. 1j. The result suggests the existence of C, Co, Zn and N elements, and further indicates the good distribution of these elements. The energy-dispersive X-ray spectroscopy (EDX) result (Fig. S4†) shows the presence of C, Co, Zn, and N, agreeing well with the elemental mapping of energy-filtered TEM. The N content in the pitaya-like microspheres estimated by EDX was roughly 5%, which was mainly derived from the nitrile groups (–C≡N) in the PBA precursor.

The high crystallinity of the pitaya-like microspheres was further confirmed by the XRD spectrum, as shown in Fig. 2a. All the diffraction peaks can be well assigned to the cubic Co_3ZnC phase (JCPDS card no. 29-0524, space group: $Pm\bar{3}m$, $a = 3.730$, $b = 3.730$, and $c = 3.730$). Raman spectroscopy was employed to identify the characteristics of carbon frameworks in the pitaya-like microspheres. As shown in Fig. 2b, two Raman peaks are observed in the range of 1000 to 2000 cm^{-1}. The Raman peak at ~1350 cm^{-1} can be ascribed to the D band, while the Raman peak at ~1590 cm^{-1} is attributed to the G band. This further proves the existence of elemental carbon in the final product.[40] The intensity ratio of the D band to G band (I_D/I_G) approaches ~1.06, implying partial graphitization.[41] Thermogravimetric analysis (TGA) was conducted under air atmosphere to evaluate the content of carbon in the final product. As shown in Fig. S5,† the weight loss was 5.9% when the temperature increased from room temperature to 250 °C, and then reached 37.8% when the temperature further increased to 600 °C. Thus, it can be concluded that the carbon content in the final product is *ca.* 31.9%. Interestingly, when the temperature increased to about 800 °C, the weight loss became 31.6%, this could be attributed to the oxidation of Co_3ZnC nanoparticles in air. To identify the

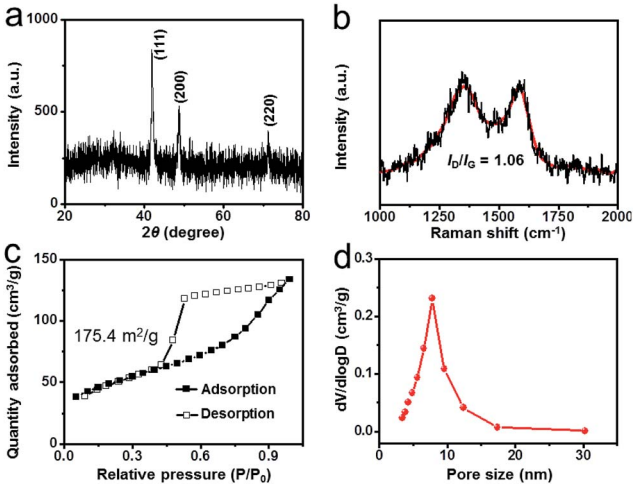

Fig. 2 Composition characterization of pitaya-like microspheres. (a) XRD spectrum, (b) Raman spectrum, (c) N_2 adsorption–desorption isotherm, and (d) pore size distribution of pitaya-like microspheres, respectively.

high-porosity characteristic of the microspheres, we investigated the specific surface area of the multicore microspheres by measuring N_2 adsorption–desorption isotherms. It can be seen from Fig. 2c that the pitaya-like microsphere possesses a specific surface area as high as 175.4 m^2 g^{-1}, and exhibits a mesoporous structure with an average pore diameter of ~7.4 nm (Fig. 2d). It is known that the porous structure is beneficial for the electrochemical properties, especially for the electrochemical process which highly depends on the penetration and migration of electrolyte ions.[42,43]

For comparison, bare Co_3ZnC nanoparticles were also prepared without the introduction of PVP in the synthesis process. As shown in Fig. S6a,† the FESEM image revealed that the control sample of the $Zn_3[Co(CN)_6]_2 \cdot nH_2O$ precursor without PVP is composed of small particles with irregular structures. After annealing, the PBA precursor converted into bare Co_3ZnC particles (Fig. S6b†), and the following TEM characterization (Fig. S6c†) revealed a size range of 10–15 nm, which is consistent with that of the encapsulated Co_3ZnC particles in pitaya-like microspheres. The EDX spectrum (Fig. S6d†) together with the corresponding elemental mapping (Fig. S6e–h†) demonstrates the co-existence of C, Co, and Zn elements, and furthermore reflects the homogeneous distribution of these elements in the product. The XRD characterization (Fig. S7†) confirmed the successful preparation of bare Co_3ZnC nanoparticles. Thus, the main structure difference is that no carbon framework is covered on the surface of bare Co_3ZnC nanoparticles, indicating that the introduction of PVP is a key factor for the formation of pitaya-like microspheres. In addition, the TGA result of bare Co_3ZnC presented in Fig. S8† also suggested the high thermal stability of Co_3ZnC at 600 °C, and further confirmed that the carbon content in pitaya-like microspheres was correctly calculated. The N_2 adsorption–desorption isotherm of bare Co_3ZnC nanoparticles was also provided (Fig. S9†), showing a specific surface area of ~87.5 cm^2 g^{-1}, which is much smaller than that of pitaya-like microspheres.

Electrochemical performance of pitaya-like microspheres

Considering the unique architecture and compositions, the resultant pitaya-like microspheres were expected to have great potential in energy storage. To compare the electrochemical performance of pitaya-like microspheres with those of reported carbon-based anode materials, the loading mass of the active material was set at 1.0–2.0 mg. We then employed both cyclic voltammetry (CV) and galvanostatic charge/discharge measurements to investigate the lithium storage performance of pitaya-like microspheres as anode materials for LIBs. The typical CV curves of pitaya-like microspheres are presented in Fig. S10,† a broad peak at around 0.78 V was observed during the first lithiation cycle, and then disappeared in the subsequent cycles. This irreversible peak may result from the formation of solid-electrolyte interphase (SEI) films. Moreover, no obvious lithiation or delithiation peaks were observed from the CV curves, this is in good agreement with that of MXene Nb_2CT_x/CNT in the literature.[17] The CV curves of the bare Co_3ZnC nanoparticle electrode (Fig. S11†) displayed similar characteristics to those of pitaya-like microspheres. Further *ex situ* XRD characterization (Fig. S12†) of pitaya-like microspheres at different charge/discharge states evidences no obvious variation in diffraction peaks, suggesting that the pitaya-like microsphere material may not follow the conventional conversion reaction mechanism. According to the previously reported studies,[44–46] Li^+ can adsorb on the surface of nanoparticles, the pores and 3D conductive carbon frameworks can also serve as reservoirs for the storage of Li^+, all these factors contribute to such an excellent Li^+ storage performance of pitaya-like microspheres.

Fig. 3a shows the typical charge/discharge profiles of pitaya-like microspheres as the anode material at the first, second, 100th and 300th cycle with a current density of 100 mA g^{-1} in a potential window of 0.01–3.0 V (*vs.* Li/Li^+). In the discharge profiles, almost no plateaus could be observed, this is consistent with the above CV results. Notably, the pitaya-like microsphere anode delivers high initial charge and discharge capacities of 607 and 908 mA h g^{-1}, respectively. The irreversible capacity and relatively low coulombic efficiency for the first cycle are mainly attributed to irreversible side reactions on the surface of the anode such as the incomplete decomposition of the as-formed SEI film.[47,48] In the subsequent cycles, the reversible capacity is 586 mA h g^{-1} in the second cycle, and can maintain a high capacity of 481 and 608 mA h g^{-1} in the 100th and 300th cycle, respectively. The cycling performance of the pitaya-like microsphere anode at a current density of 100 mA g^{-1} was investigated, as shown in Fig. 3b. From the first cycle onward, the discharge capacity of the pitaya-like microsphere anode decreased to 381 mA h g^{-1} at the 44th cycle, then increased to 578 mA h g^{-1} at the 200th cycle, and later delivered a capacity of 608 mA h g^{-1} at the 300th cycle, corresponding to 67.0% retention of the initial discharge capacity. The decrement of discharge capacity at the initial cycles can be attributed to the

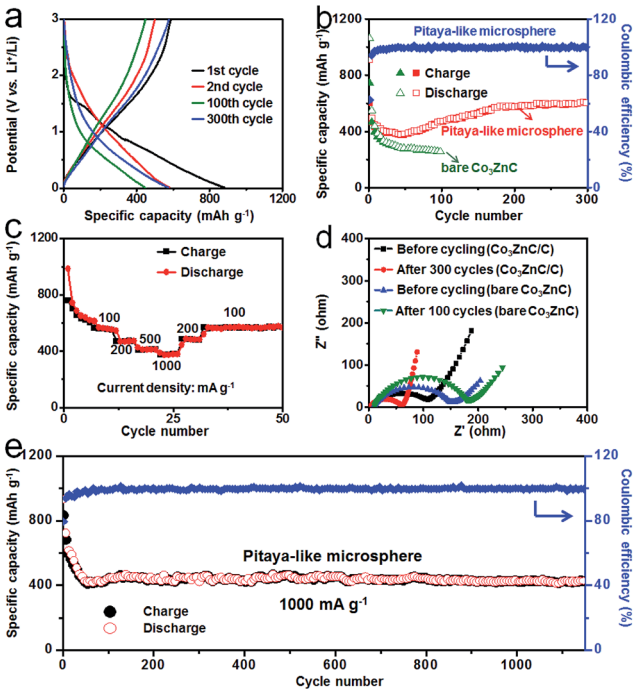

Fig. 3 Electrochemical performance of pitaya-like microspheres. (a) Charge/discharge profiles of pitaya-like microspheres as anode materials of LIBs at 100 mA g^{-1}. (b) Cycling performance comparison of pitaya-like microspheres and bare Co_3ZnC nanoparticles, and the corresponding coulombic efficiency of pitaya-like microspheres at 100 mA g^{-1}. (c) Rate performance of pitaya-like microspheres at various current densities ranging from 100 to 1000 mA g^{-1}. (d) Nyquist plots of pitaya-like microspheres and bare Co_3ZnC nanoparticles at the initial cycle and after long-term cycling tests. (e) Cycling performance and the corresponding coulombic efficiency of pitaya-like microspheres at 1000 mA g^{-1}.

formation of a polymeric gel-like SEI layer resulting from electrolyte degradation during the activation process, and the later increase of discharge capacity can be ascribed to the dissolution of the SEI film as well as the finish of the activation process. This phenomenon can also be found in other electrode materials.[49,50] In sharp contrast, the bare Co_3ZnC nanoparticle anode exhibits a similar initial charge/discharge profile compared to that of pitaya-like microspheres (Fig. S13†), but with much inferior cycling stability after only 100 cycles (257 mA h g^{-1} at the 100th cycle, as shown in Fig. 3b).

The rate capability of the pitaya-like microsphere anode was evaluated at different current densities ranging from 100 to 1000 mA g^{-1}. As shown in Fig. 3c, the specific capacities are *ca.* 569, 470, 412 and 377 mA h g^{-1} at current densities of 100, 200, 500, and 1000 mA g^{-1}, respectively. When the current density is restored to 100 mA g^{-1}, the discharge capacity resumes to 567 mA h g^{-1}. The rate capability of pitaya-like microspheres was also tested with different cells at various current densities, as presented in Fig. S14.† The discharge capacities of the pitaya-like microsphere electrode at 200, 500, and 1000 mA g^{-1} after 50 cycles are 537, 448 and 402 mA h g^{-1}, respectively. These values are almost identical to those in Fig. 3c, further suggesting the great rate capability of pitaya-like microspheres. The rate performance of bare Co_3ZnC nanoparticles was also provided for comparison. As shown in Fig. S15,† when the current density increased to 1000 A g^{-1}, the bare Co_3ZnC nanoparticle anode delivered a low specific capacity of 64 mA h g^{-1}. This result suggests that the pitaya-like microspheres exhibit much better rate performance than bare Co_3ZnC nanoparticles, which should be attributed to the different architecture of these two materials (see ESI S1† for more discussion). As another control experiment, we have prepared bare carbon frameworks (Fig. S16†) by completely removing the Co_3ZnC nanoparticles in pitaya-like microspheres through the etching of HF (5 wt%) and HCl (1.0 M) successively. As detailed in the ESI,† it is confirmed that the contribution of carbon frameworks to the overall capacity of the pitaya-like microspheres is limited due to the relatively small surface area (316.5 cm^2 g^{-1}, Fig. S17†), small pore volume (0.53 cm^3 g^{-1}, Fig. S17†), relatively low specific capacity (436 mA h g^{-1}, Fig. S18a†) and low mass content (~31.9 wt% according to the TGA result in Fig. S5†). It indicates that the Co_3ZnC material provides the main contribution to lithium storage, while the porous and 3D conductive carbon framework can greatly enhance the long-term stability and cycling performance of the Co_3ZnC based anode.

In order to figure out the differences of internal electrical resistance behind the discrepant lithium storage performance, EIS measurements were conducted. Fig. 3d presents the Nyquist plots of pitaya-like microspheres and bare Co_3ZnC nanoparticles before and after long-term cycling tests. It is shown that all of the Nyquist plots exhibit the same shape, which consists of a semicircle and an incline. The semicircle diameter of the pitaya-like microspheres before long-term cycling is much smaller than that of bare pitaya-like microspheres, implying that the contact and charge-transfer impedance of the pitaya-like microspheres anode is lower than that of bare Co_3ZnC nanoparticles. After the long-term stability test, the contact and charge-transfer impedance of pitaya-like microspheres decreased greatly, while the charge-transfer impedance of bare Co_3ZnC nanoparticles increased. These prove that the pitaya-like microspheres have better electronic conductivity and charge-transfer performance than the bare Co_3ZnC nanoparticles before or after long-term cycling tests. This phenomenon can be attributed to the existence of a 3D porous and conductive carbon matrix in pitaya-like microspheres, which leads to the gradual activation process and the wetting of 3D porous carbon frameworks with the electrolyte after long-term cycling that can decrease the contact resistance and charge-transfer impedance.[51,52]

To investigate the structural stability of pitaya-like microspheres, the anode was evaluated by a long-term cycling test at a high current density of 1000 mA g^{-1}, as shown in Fig. 3e. The initial discharge and charge capacity was 930 and 831 mA h g^{-1}, respectively. From the second cycle onward, the specific capacity decreased and reached 417 mA h g^{-1} at the 80th cycle. Thereafter, the pitaya-like microsphere anode delivered a high discharge capacity of 423 mA h g^{-1} even after 1150 consecutive cycles, indicating its exceptional cycling stability. It should be noted that the pitaya-like microsphere electrode displayed a minimum capacitance at 100 mA g^{-1} (381 mA h g^{-1} in the 44th

cycle) even smaller than that at 1000 mA g^{-1} (417 mA h g^{-1} in the 80th cycle). This phenomenon is attributed to the slower formation of the SEI layer at lower current density as well as the slower activation process at lower current density, which also can be observed from some other anode materials in the literature.[53–56] These results suggest that the pitaya-like microsphere anode can maintain extraordinary stability under high-rate cycling, which is very beneficial to practical applications. In addition, compared to the lithium storage performance of other previously reported carbide materials, such as MXene Nb_2CT_x/CNT (420 mA h g^{-1} at 0.5C),[17] $Ti_3C_2T_x$ (~150 mA h g^{-1} at 30 mA g^{-1}),[57] Ti_2C (160 mA h g^{-1} at 0.1C)[58] and Ti_3C_2 (126 mA h g^{-1} at 1C),[59] the pitaya-like microsphere anode demonstrated in this work exhibited superior capacity, rate capability and long-term stability (423 mA h g^{-1} at 1000 mA g^{-1} after 1150 cycles). The morphology of pitaya-like microspheres after the long-term cycling test was also investigated. As shown in Fig. S19a and b,† the morphology and microstructure of pitaya-like microspheres maintained well in terms of shape, size and structural integrity after 1150 cycles at 1000 mA g^{-1}. In contrast, the FESEM observation of bare Co_3ZnC nanoparticles (Fig. S19c and d†) after 100 cycles at 100 mA g^{-1} revealed the serious aggregation leading to a poor electrochemical performance. It proves that the encapsulation of Co_3ZnC nanoparticles within a conductive carbon framework can effectively prevent the degradation of structural integrity and electrochemical performance after long-term stability tests.

According to the XPS analysis of pitaya-like microspheres (Fig. S20†), the N content was measured to be 4.8 wt%. To investigate the influence of N-doping on the lithium storage performance, control experiments were carried out. After the complete removal of Co_3ZnC nanoparticles in pitaya-like microspheres, the XPS result demonstrated that the N content in the resultant bare carbon frameworks is about 13.1 wt% (Fig. S21a†). Moreover, the bare carbon framework electrode displays a low discharge capacity of about 436 mA h g^{-1} after 20 cycles at 100 mA g^{-1} (Fig. S18a†). The bare carbon frameworks were further thermally annealed at 1000 °C for 6 h to eliminate the N species. The XPS result shows almost no N species (0.3 wt%) in the annealed product, as shown in Fig. S21b.† Further electrochemical tests reveal that the product exhibited a discharge capacity of about 414 mA h g^{-1} after 20 cycles at 100 mA g^{-1} (Fig. S18b†), slightly lower than that of bare carbon frameworks before 1000 °C annealing. Therefore, the influence of N-doping on the lithium storage performance of pitaya-like microspheres is limited.

Based on the above observation and analysis, it can be concluded that the exceptional Li^+ storage performance of the pitaya-like microsphere material is closely related to its unique 3D architecture, as illustrated in Fig. 4a. To confirm this, further TEM characterization at different charge/discharge states was performed to understand the structural and morphological changes of pitaya-like microspheres during the electrochemical measurements, as shown in Fig. 4b–e. The 3D carbon frameworks can buffer the volume change, prevent the aggregation of Co_3ZnC nanoparticles and restrict the formation of the SEI layer to the outside of carbon frameworks, as evidenced by Fig. 4c–e.

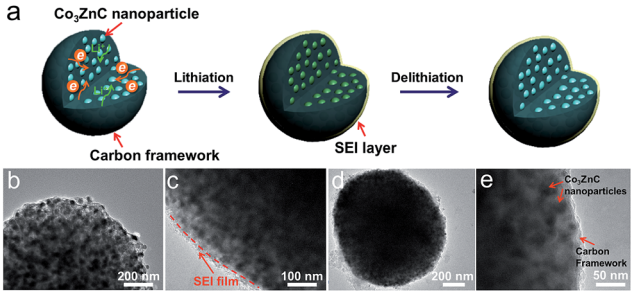

Fig. 4 (a) Schematic illustration of the pitaya-like microspheres during lithiation/delithiation processes. (b–e) TEM images of pitaya-like microspheres (b) before and (c–e) after different charge/discharge cycles. (c) The thin SEI layer was generated and restricted to the outside of the 3D porous carbon framework in the delithiation process after 10 cycles at 100 mA g^{-1}. (d) The structural integrity of pitaya-like microspheres maintained well at the full lithiation state after 1150 charge/discharge cycles at 1000 mA g^{-1}. (e) The distribution of Co_3ZnC nanoparticles in the carbon framework at the full lithiation state after 1150 cycles at 1000 mA g^{-1}.

In the delithiation process, the structure of pitaya-like microspheres was soundly restored except the formation of the SEI layer on the surface of the carbon framework (Fig. 4c). Even at the full lithiation state after 1150 charge/discharge cycles, the volume expansion of Co_3ZnC/C cores reached a maximum value but still could not break the carbon framework, and the morphology of pitaya-like microspheres maintained well (Fig. 4d), suggesting the high structural integrity of the pitaya-like microspheres. Moreover, the Co_3ZnC particles and carbon framework can be clearly identified (Fig. 4e), and the Co_3ZnC nanoparticles are still distributed uniformly in the 3D carbon frameworks without no obvious aggregation, demonstrating the ultrahigh stability of pitaya-like microspheres for the application of LIBs. In addition, the mesoporous nanostructure can act as a reservoir for the storage of Li^+, and it is beneficial to the fast infiltration and diffusion of the electrolyte, providing short path lengths with less resistance for both Li^+ and electron transport within the electrolyte.[45,60] These results demonstrate that the unique architecture of pitaya-like microspheres is responsible for the excellent Li^+ storage performance.

Conclusions

In summary, we have prepared pitaya-like microspheres with carbide nanoparticles embedded in mesoporous spherical carbon frameworks *via* a facile and effective strategy, which consisted of an ultrasonication-assisted solution-phase approach and a subsequent thermal annealing process. Owing to their unique structural features and desirable compositions, the resultant porous pitaya-like microspheres exhibit excellent electrochemical performances when evaluated as anodes for LIBs. Remarkably, it demonstrates that the cyclic performance and long-term stability of anodes can be significantly improved by the greatly enhanced structural integrity. We suggest that the simple synthesis approach proposed in this work could be widely applied in the preparation of other metal carbide/carbon

composites for next-generation LIBs, as well as other energy storage systems.

Acknowledgements

This work was supported by the National Thousand Young Talents Program of China, the Young Scientists Project of National Basic Research Program of China (973 Program No. 2015CB659300), the National Natural Science Foundation of China (NSFC Grant No. 21403105; No. 21573108), the China Postdoctoral Science Foundation (Grant No. 2015M581769; No. 2015M580413; No. 2015M581775; No. 2015M580408), the Jiangsu Province Science Foundation for Youths (Project No. BK20150571; No. BK20150583), the Fundamental Research Funds for the Central Universities and a project funded by the Priority Academic Program Development of Jiangsu Higher Education Institutions (PAPD).

Notes and references

1 P. Simon and Y. Gogotsi, *Nat. Mater.*, 2008, **7**, 845–854.
2 A. S. Arico, P. Bruce, B. Scrosati, J. M. Tarascon and W. Schalkwijk, *Nat. Mater.*, 2005, **4**, 366–377.
3 P. G. Bruce, B. Scrosati and J. M. Tarascon, *Angew. Chem., Int. Ed.*, 2008, **47**, 2930–2946.
4 B. Dunn, H. Kamath and J. M. Tarascon, *Science*, 2011, **334**, 928–935.
5 M. R. Gao, Y. F. Xu, J. Jiang and S. H. Yu, *Chem. Soc. Rev.*, 2013, **42**, 2986–3017.
6 J. M. Tarasco and M. Armand, *Nature*, 2001, **414**, 359–367.
7 B. Kang and G. Ceder, *Nature*, 2009, **458**, 190–193.
8 P. Poizot, S. Laruelle, S. Grugeon, L. Dupont and J. M. Tarascon, *Nature*, 2000, **407**, 496–499.
9 J. B. Goodenough and Y. Kim, *Chem. Mater.*, 2010, **22**, 587–603.
10 E. J. Yoo, J. Kim, E. Hosono, H. S. Zhou, T. Kudo and I. Honma, *Nano Lett.*, 2008, **8**, 2277–2282.
11 Y. G. Guo, J. S. Hu and L. J. Wan, *Adv. Mater.*, 2008, **20**, 2878–2887.
12 W. Y. Li, L. N. Xu and J. Chen, *Adv. Funct. Mater.*, 2005, **15**, 851–857.
13 C. K. Chan, H. L. Peng, G. Liu, K. Mcilwrath, X. F. Zhang, R. A. Huggins and Y. Cui, *Nat. Nanotechnol.*, 2008, **3**, 31–35.
14 C. Liu, F. Li, L. P. Ma and H. M. Cheng, *Adv. Mater.*, 2010, **22**, E28–E62.
15 S. B. Yin, M. Cai, C. X. Wang and P. K. Shen, *Energy Environ. Sci.*, 2011, **4**, 558–563.
16 M. Naguib, J. Halim, J. Lu, K. M. Cook, L. Hultman, Y. Gogotsi and M. W. Barsoum, *J. Am. Chem. Soc.*, 2013, **135**, 15966–15969.
17 O. Mashtalir, M. R. Lukatskaya, M. Q. Zhao, M. W. Barsoum and Y. Gogotsi, *Adv. Mater.*, 2015, **27**, 3501–3506.
18 Y. Xie, Y. DallAgnese, M. Naguib, Y. Gogotsi, M. W. Barsoum, H. L. Zhuang and P. R. C. Kent, *ACS Nano*, 2014, **8**, 9606–9615.
19 H. Huang, T. Feng, Y. Gan, M. Y. Fang, Y. Xia, C. Liang, X. Y. Tao and W. K. Zhang, *ACS Appl. Mater. Interfaces*, 2015, **7**, 11842–11848.
20 J. P. Hu, B. Xu, C. Y. Ouyang, S. Y. A. Yang and Y. Yao, *J. Phys. Chem. C*, 2014, **118**, 24274–24281.
21 C. Eames and M. S. Islam, *J. Am. Chem. Soc.*, 2014, **136**, 16270–16276.
22 Q. Tang, Z. Zhou and P. W. Shen, *J. Am. Chem. Soc.*, 2012, **134**, 16909–16916.
23 M. R. Lukatskaya, O. Mashtalir, C. E. Ren, Y. Dall'Agnese, P. Rozier, P. L. Taberna, M. Naguib, P. Simon, M. W. Barsoum and Y. Gogotsi, *Science*, 2013, **341**, 1502.
24 H. W. Wang, Y. Zhang, H. X. Ang, Y. Q. Zhang, H. T. Tan, Y. F. Zhang, Y. Y. Guo, J. B. Franklin, X. L. Wu, M. Srinivasan, H. J. Fan and Q. Y. Yan, *Adv. Funct. Mater.*, 2016, **26**, 3082–3093.
25 H. Huang, T. Feng, Y. Gan, M. Fang, Y. Xia, C. Liang, X. Tao and W. Zhang, *ACS Appl. Mater. Interfaces*, 2015, **7**, 11842–11848.
26 Y. Zhong, X. H. Xia, F. Shi, J. Y. Zhan and J. P. Tu, *Adv. Sci.*, 2016, **3**, 1500286.
27 X. Y. Lang, A. Hirata, T. Fujita and M. W. Chen, *Nat. Nanotechnol.*, 2011, **6**, 232–236.
28 L. W. Ji, Z. Lin, M. Alcoutlabi and X. W. Zhang, *Energy Environ. Sci.*, 2011, **4**, 2682–2699.
29 A. Jahel, C. M. Ghimbeu, L. Monconduit and C. Vix-Guterl, *Adv. Energy Mater.*, 2014, **4**, 1400025.
30 N. Liu, Z. D. Lu, J. Zhao, M. T. McDowell, H. W. Lee, W. T. Zhao and Y. Cui, *Nat. Nanotechnol.*, 2014, **9**, 187–192.
31 C. N. He, S. Wu, N. Q. Zhao, C. S. Shi, W. Z. Liu and J. J. Li, *ACS Nano*, 2013, **7**, 4459–4469.
32 Y. Xiao, L. R. Zheng and M. H. Cao, *Nano Energy*, 2015, **12**, 152–160.
33 X. N. Li, J. W. Liang, Z. G. Hou, W. Q. Zhang, Y. Wang, Y. C. Zhu and Y. T. Qian, *Adv. Funct. Mater.*, 2015, **25**, 5229–5238.
34 G. Lui, G. Li, X. L. Wang, G. P. Jiang, E. Lin, M. Fowler, A. P. Yu and Z. W. Chen, *Nano Energy*, 2016, **24**, 72–77.
35 N. Mahmood, J. H. Zhu, S. Rehman, Q. Li and Y. L. Hou, *Nano Energy*, 2015, **15**, 755–765.
36 J. X. Guo, L. Chen, G. J. Wang, X. Zhang and F. F. Li, *J. Power Sources*, 2014, **246**, 862–867.
37 L. B. Ma, X. P. Shen, J. Zhu, G. X. Zhu and Z. Y. Ji, *J. Mater. Chem. A*, 2015, **3**, 11066–11073.
38 B. Zhao, S. Y. Huang, T. Wang, K. Zhang, M. M. F. Yuen, J. B. Xu, X. Z. Fu, R. Sun and C. P. Wong, *J. Power Sources*, 2015, **298**, 83–91.
39 T. Chen, Y. Hu, B. R. Chen, R. P. Chen, H. L. Lv, L. B. Ma, G. Y. Zhu, Y. R. Wang, C. Z. Yan, Z. X. Tie, Z. Jin and J. Liu, *Nano Energy*, 2016, **20**, 305–314.
40 L. F. Chen, X. D. Zhang, H. W. Liang, M. G. Kong, Q. F. Guan, P. Chen, Z. F. Wu and S. H. Yu, *ACS Nano*, 2012, **6**, 7092–7102.
41 J. N. Zhang, K. X. Wang, Q. Xu, Y. C. Zhou, F. Y. Cheng and S. J. Guo, *ACS Nano*, 2015, **9**, 3369–3376.

42 S. J. Peng, L. L. Li, H. T. Tan, R. Cai, W. H. Shi, C. C. Li, S. G. Mhaisalkar, M. Srinivasan, S. Ramakrishna and Q. Y. Yan, *Adv. Funct. Mater.*, 2014, **24**, 2155–2162.

43 Y. B. Zhang and Z. G. Guo, *Chem. Commun.*, 2014, **50**, 3443–3446.

44 K. Z. Cao, L. F. Jiao, H. Xu, H. Q. Liu, H. Y. Kang, Y. Zhao, Y. C. Liu, Y. J. Wang and H. T. Yuan, *Adv. Sci.*, 2015, 1500185.

45 Z. Li, Z. W. Xu, X. H. Tan, H. L. Wang, C. M. B. Holt, T. Stephenson, B. C. Olsen and D. Mitlin, *Energy Environ. Sci.*, 2013, **6**, 871–878.

46 R. Mukherjee, A. V. Thomas, D. Datta, E. Singh, J. W. Li, O. Eksik, V. B. Shenoy and N. Koratkar, *Nat. Commun.*, 2014, **5**, 3710–3719.

47 L. W. Su, Z. Zhou and P. W. Shen, *Electrochim. Acta*, 2013, **87**, 180–185.

48 J. Bai, X. G. Li, G. Z. Liu, Y. T. Qian and S. L Xiong, *Adv. Funct. Mater.*, 2014, **24**, 3012–3020.

49 J. Vetter, P. Novak, M. R. Wagner, C. Veit, K. C. Moller, J. O. Besenhard, M. Winter, M. Wohlfahrt, C. Vogler and A. Hammouche, *J. Power Sources*, 2005, **147**, 269–281.

50 F. Han, D. Li, W. C. Li, C. Lei, Q. Sun and A. H. Lu, *Adv. Funct. Mater.*, 2013, **23**, 1692–1700.

51 Y. Xia, Z. Xiao, X. Dou, H. Huang, X. H. Lu, R. J. Yan, Y. P. Gan, W. J. Zhu, J. P. Tu, W. K. Zhang and X. Y. Tao, *ACS Nano*, 2013, **7**, 7083–7092.

52 C. Wang, W. Wan, Y. H. Huang, J. T. Chen, H. H. Zhou and X. X. Zhang, *Nanoscale*, 2014, **6**, 5351–5358.

53 P. Xiong, B. R. Liu, V. Teran, Y. Zhao, L. L. Peng, X. Wang and G. H. Yu, *ACS Nano*, 2014, **8**, 8610–8616.

54 G. B. Zeng, N. Shi, M. Hess, X. Chen, W. Cheng, T. X. Fan and M. Niederberger, *ACS Nano*, 2015, **9**, 4227–4235.

55 L. Pan, X. D. Zhu, X. M. Xie and Y. T. Liu, *Adv. Funct. Mater.*, 2015, **25**, 3341–3350.

56 H. J. Zhang, K. X. Wang, X. Y. Wu, Y. M. Jiang, Y. B. Zhai, C. Wang, X. Wei and J. S. Chen, *Adv. Funct. Mater.*, 2014, **24**, 3399–3404.

57 S. J. Kim, M. Naguib, M. Q. Zhao, C. F. Zhang, H. T. Jung, M. W. Barsoum and Y. Gogotsi, *Electrochim. Acta*, 2015, **163**, 246–251.

58 J. Come, M. Naguib, P. Rozier, M. W. Barsoum, Y. Gogotsi, P. L. Taberna, M. Morcrette and P. Simon, *J. Electrochem. Soc.*, 2012, **159**, A1368–A1373.

59 D. D. Sun, M. S. Wang, Z. Y. Li, G. X. Fan, L. Z. Fan and A. G. Zhou, *Electrochem. Commun.*, 2014, **47**, 80–83.

60 R. Mukherjee, A. V. Thomas, D. Datta, E. Singh, J. W. Li, O. Eksik, V. B. Shenoy and N. Korarkar, *Nat. Commun.*, 2014, **5**, 3710–3719.